Sustainable Materials and Technologies 32 (2022) e00419

Contents lists available at ScienceDirect

Sustainable Materials and Technologies

journal homepage: www.elsevier.com/locate/susmat

Microwave-assisted self-template synthesis of mesoporous anatase TiO_2 spheres for non-aqueous Al-ion batteries: Textural property optimization and enhanced reversible Al^{3+} storage

Dongwei Ma [a], Linyunuo Lai [a], Carlos Ponce de León [b], Du Yuan [c], Jia Hong Pan [a,*]

[a] MOE Key Laboratory of Resources and Environmental Systems Optimization, College of Environmental Science and Engineering, North China Electric Power University, Beijing 102206, China
[b] Faculty of Engineering and Physical Sciences, University of Southampton, Highfield, Southampton SO17 1BJ, United Kingdom
[c] College of Materials Science and Engineering, Changsha University of Science and Technology, Changsha 410004, Hunan, China

ARTICLE INFO

Keywords:
Mesoporous anatase TiO_2 spheres
Electrochemical energy storage
Aluminium-ion batteries
Ionic liquid electrolyte
Microwave-induced hydrothermal crystallization

ABSTRACT

Mesoporous anatase TiO_2 spheres (MATS) are elaborated *via* microwave-assisted rapid crystallization of hydrous TiO_2 colloidal spheres (HTCS) self-template. Tuning the hydrothermal and calcination temperatures allow for textural property-controllable synthesis. The optimal MATS are demonstrated as a promising cathode material of aluminium-ion batteries (AIBs) and show superior rate and capacity performances. Their large surface area and porous structure offer a robust and interconnected scaffold for Al^{3+} insertion/exertion with higher reversibility. The constructed non-aqueous AIBs with RTILs electrolyte deliver the highest initial capacity of 145.3 mA h g^{-1} at 0.2C with high Coulombic efficiency of ≈ 96.5%, and a reversible capacity of 78.0 mA h g^{-1} at 1C can be retained after 200 cycles with high Coulombic efficiency of ≈ 98.6%. Our study on the Al storage mechanism further shows the charge/discharge process involves the extraction/insertion of Al species (Al^{3+}, $AlCl_4^-$, $Al_2Cl_7^-$, *etc.*) into the TiO_2 crystal lattices with the formation of intermediate aluminium titanium oxides ($Al_2Ti_7O_{15}$ and Al_2TiO_5) and non-oxides ($Ti(AlCl_4)_2$ and $Ti(ClO_4)_4$). The continuous enrichment of the latter during cycling greatly deteriorates the reversibility of AIBs.

1. Introduction

With the evolving energy demand, lithium-ion batteries (LIBs) have achieved unprecedented developments in the past two decades [1–3]. However, the limited lithium resource and the high cost of raw lithium materials motivate the research progress of other multivalent-ion batteries (MIBs) [4–8]. Among various MIBs, aluminium-ion batteries (AIBs) are an appealing candidate for stationary energy storage due to their cost-efficient, high safety, and environmental friendliness [9–11]. Due to the three-electron transfer during the cyclic process, AIBs can exhibit high volumetric and gravimetric capacities (8046 mA h cm^{-3} *vs.* 2062 mA h cm^{-3} for LIBs and 2980 mA h g^{-1} *vs.* 3861 mA h g^{-1} for LIBs) [12]. And the facile electrodeposition/stripping process of Al metal in room temperature ionic liquids (RTILs) determines that it can be directly utilized as anode for non-aqueous aluminium ion batteries (NAIBs) in the form of a metallic foil [13,14]. However, contrary to monovalent such as Li^+, Na^+, and K^+, it is difficult for Al^{3+} to embed or escape in the host cathode materials because of the strong Coulombic interaction derived from high valence state and small radius (0.59 Å) bonding with anions [15].

Up to now, various energy materials have been studied as such as carbon [16–18], transition metal oxides [19,20], sulfides [21–23], selenides [24,25], tellurides [26], Prussian blue analogs [27], polyanion compounds [28], covalent organic frameworks (COFs) [29], 2D carbides and nitrides (Mxenes) [30], and organic polymer [31], of which TiO_2 is particularly interesting owing to its low cost, environmental benignity, excellent corrosion resistance, and high specific capacity [32–35]. The pioneering efforts were devoted to the aqueous AIBs (AAIBs) [36]. Porous TiO_2 nanotubes have been demonstrated efficient insertion/extraction of small radius steric effect of Al^{3+} [37,38], and the underlying reversible phase transitions from TiO_2 to aluminium titanate (Al_2TiO_5) through *ex-situ* XRD technology during the cycling process were reported in the AAIBs [39]. These studies showed the validity of TiO_2 cathodes for AAIBs, but their electrochemical performance is

* Corresponding author.
E-mail address: pan@ncepu.edu.cn (J.H. Pan).

https://doi.org/10.1016/j.susmat.2022.e00419
Received 25 December 2021; Received in revised form 3 February 2022; Accepted 5 March 2022
Available online 9 March 2022
2214-9937/© 2022 Elsevier B.V. All rights reserved.

generally inferior [40]. Inevitable self-discharge, poor capacity, and low working voltage are widely present in the fabricated AAIBs.

Alternatively, non-aqueous AIBs (NAIBs) show promises in improving the Al ion storage properties, in which the most employed electrolyte is room-temperature ionic liquids (RTILs), such as $AlCl_3$/[EMIm]Cl (1-Ethyl-3-methylimidazolium chloride) [41], $AlCl_3$/urea [42], $AlCl_3$/acetamide [43], $AlCl_3$/trimethylamine [44], $AlCl_3$/4-ethylpyridine [45] and $AlCl_3/Et_3NHCl$ [46]. RTILs inhibit side reactions of hydrogen evolution and increase the electron and ion transports thanks to their highly ionic conductivity [47]. Accordingly, a few reports have emerged to explore TiO_2 as NAIB cathode for Al^{3+} ion storage. For instance, Koketsu et al. [48] used Ti-deficient TiO_2 cathode to accommodate Al ions in NAIBs with $AlCl_3$/[EMIm]Cl (molar ratio: 1.1/1.0) as the electrolyte. The cationic deficiency reduces the Coulombic forces inside the lattice, and increases the initial capacity from 30 to 120 mA h g^{-1}, compared with the pristine TiO_2, although the long-term stability is not satisfactory owing to the inreversable transformation in crystal structure during the cyclic charge/discharge process. Wang et al. [49] employed high-conductivity TiN (22.5 wt%) to improve the electrochemical properties of anatase TiO_2 nanorods. The composites delivered an initial discharge capacity of 73 mA h g^{-1} at a constant current of 0.5 A g^{-1} (≈1.5C) and stabilized in the first 100 cycles in the NAIBs with the $AlCl_3$/[EMIm]Cl RTIL electrolyte. However, the long-term performance is still low based on the currently developed low-dimensional TiO_2 nanostructures. The insertion/exsertion of Al^{3+} ions leads to the dramatical expansion/shrinkage of anatase crystal structure, eventually resulting in capacity loss.

From nanostructure point view, mesoporous anatase TiO_2 spheres (MATS) consisting of nanocrystallites might be a promising candidate. Recent progress has demonstrated that their excellent photo/electrochemical performance benefit from their well-defined hierarchical structure: the spherical morphology being helpful for packing, and their interconnected nanocrystallites and the built-up voids offering high-conductivity and high-porosity scaffolds for charge transfer and ion transformation during the cyclic electrochemical charge/discharge process, as well verified in LIBs recently [50]. Therefore, through carefully tuning the porous structure, MATS-based NAIBs might enable to boost the long-term stability and capacity performance. In this work, we firstly report a facile microwave-assisted self-template synthesis strategy for the rapid crystallization of MATS. We then demonstrate the efficient Al ion storage properties of MATS. The optimal one exhibits the highest initial capacity of 145.3 mA h g^{-1} at 0.2C and 78.0 mA h g^{-1} at 1C after 200 cycles with high Coulombic efficiency of ≈98.6%. Finally, the underlying Al ion storage mechanism in MATS is explored, with a special emphasis on emphasis on the electrodeposition of Al and the evolution of chlorine gas (Cl_2) during the cycling processes.

2. Experimental

2.1. Materials

All the chemicals were purchased from Sigma-Aldrich, Alfa Aesar, and Merck, and used as received without further purification except that titanium (IV) tetraisopropoxide (TTIP, >97 wt%) was distilled under the reduced pressure at 120 °C before use [51–53]. After distillation, the yellow TTIP became colorless and highly transparent. The 1-ethyl-3-methylimidazolium chloride ([EMIm]Cl, 97%) was baked at 130 °C under vacuum for 48 h to remove residual water. All the employed organic solvents were HPLC-grade.

2.2. Hydrous TiO_2 colloidal spheres (HTCS) synthesized by sol-gel process

As Scheme S1 shows, 4.0 mL of distilled TTIP promptly into a mixed solvent containing ethanol (96.0 g), acetonitrile (64.0 g), DI water (0.728 mL), and $NH_3{\cdot}H_2O$ (0.034 mL, ~28%) under vigorous stirring at room temperature [51–53]. Within 5 s, a white precipitate was generated gradually. After 5–6 min, the suspension was aged for 2 h under gentle stirring. After centrifugation and washed process (wash 3 times with alcohol and DI water, respectively), uniform amorphous HTCS were obtained.

2.3. Microwave-assisted self-templated synthesis of MATS

1.0 g HCTS were redispersed in water (25 mL) and the suspension was subjected to microwave irradiation for 30 min in the CEM Discover SP equipment (Power: 150 W) under gentle stirring. Different reaction temperatures of 110, 130, and 160 °C were investigated to optimize the microwave condition. Accordingly, the resultant microwave-irradiated MATS was denoted as MATS-110, MATS-130, MATS-160 respectively.

After microwave-induced crystallization, MATS were calcined in air to fully crystalize and remove the surface organic contaminants. Typically, the optimal MATS-130 was then placed in a crucible and heated in air at 350, 450, or 550 °C for 2 h with a heating rate of 5 °C min^{-1}, and the samples were denoted as MATS-350, MATS-450, and MATS-550, respectively.

2.4. Material characterization

The crystallographic structure of MATS powder was examined by powder wide-angle X-ray diffraction (XRD) using Rigaku SmartLab SE X-ray diffractometer with a monochromated high-intensity Cu Kα radiation ($\lambda = 1.5418$ Å) with a scanning rate of 5 ° min^{-1}. The *ex-situ* XRD measurement condition of the MATS electrode was conducted with a scanning rate of 0.5 ° min^{-1}, and Kapton film (7 μm) was used to cover the electrode to prevent deterioration in the air. A Rietveld refinement with GSAS (General Structure Analysis System) was performed using the structural parameters of MATS in the anatase structure. The morphology and microstructure of MATS samples were observed by JSM-7800F scanning electron microscope (SEM) with an Oxford X-MAX50 energy dispersive spectrometer (EDS) and JEOL JEM-2010 transmission electron microscope (TEM). XPS spectra were characterized on ESCALAB 250Xi (Thermo Fisher Scientific Inc., USA) with Al-K_α radiation (72 W, 12 kV) at a pressure of 10^{-9} Torr. N_2 adsorption-desorption isotherms were obtained using a Micromeritics ASAP 2020 surface area and porosity analyzer. All samples were outgassed under vacuum for 8 h at 120 °C before measurements. Brunauer-Emmett-Teller (BET) equation was used to estimate the surface area from adsorption data obtained at $P/P_0 = 0.01$–0.30. The average pore diameters of HTCS and MATS were calculated using the *t*-plot method and Barrett-Joyner-Halenda (BJH) method from the desorption branch of the isotherm, respectively [54].

2.5. Swagelok cell assembly and electrochemical property study

The slurry of the working cathode was composed of 80 wt% MATS powder, 10 wt% carbon black, and 10 wt% polyvinylidene fluoride (PVDF) mixing in N-Methyl-2-pyrrolidone (NMP). The slurry was then uniformly coated on a current collector (Mo foil, 99.995%) and dried in vacuum at 120 °C for 12 h, and rolled twice using a rolling press (MTI MSK-HRP-MR100DC). Then the foil was cut to a round disk with a diameter of 12 mm. The loading weight of active TiO_2 cathodic materials on the disk was controlled to 1.2–1.3 mg, corresponding to the average area loading of 1.1 mg cm^{-2}.

A standard Swagelok cell (JYG-10, Zhongke Wanyuan Technology) was used for the electrochemical study of NAIBs. Cells were assembled in an argon-filled glove-box ($H_2O \leq 0.01$ ppm, $O_2 \leq 0.01$ ppm) using Al foil (99.999%) and Whatman GF/D glass fiber filter as the anode and separator, respectively. A RTIL of $AlCl_3$/[EMIm]Cl (1.3:1.0 molar ratio), which was made by mixing anhydrous aluminium chloride ($AlCl_3$, 99.999%) and [EMIm]Cl (97%, after removing residual water) with the mole ratio of 1.3:1.0 in a glove-box, was used as the electrolyte.

All the assembled cells were charged and discharged within a voltage

range of 0.2–2.4 V on a Neware battery testing system (Model: BTS-XWJ-6.44S-00052) at room temperature with diverse discharge rates from 0.5 to 10C (1C = 335 mA h g^{-1}). Cyclic voltammetry (CV) curves were recorded on an electrochemical workstation (CHI 760E, CH Instruments) at a scanning rate of 0.5 mV s^{-1}. Electrochemical impedance spectroscopy (EIS) measurement was performed on a ZIVE MP1 impedance analyzer (WonATechCorp., Korea) from 200 kHz to 5 mHz at ±5 mV where was applied as the sinusoidal perturbation. Galvanostatic intermittent titration technique (GITT) curves were recorded on the Neware battery testing system (Model: BTS-XWJ-6.44S-00052) at the 5th cycle with a constant current density of 0.2C and each pulse lasts 300 s followed by 600 s of rest.

3. Results and discussion

3.1. Textural property control of MATS

Our synthesis starts from the preparation of HTCS by the forced hydrolysis of TTIP in the mixed EtOH–ACN–H_2O medium containing a small amount of NH_3. Herein NH_3 acts as the precipitation prompter and morphological controller to guide the spontaneous self-assembly of nanosized TiO_2 hydrates to submicrospheres through hydrogen bonding, as we studied before [53,55,56]. The resultant HTCS is amorphous without any diffraction peaks in the wide-angle range (see Fig. 1a). The submicrospheres are uniform and monodisperse with an average diameter of ≈480 nm (Fig. 2a, b). The nanosized TiO_2 hydrates are closely packed, among which numerous voids form and thus create a highly porous structure, as recorded at the edge of HTCS by TEM (Fig. 2c,d). N_2 sorption analysis confirms an ultrahigh BET surface area of 337.3 m^2 g^{-1} in HTCS (Table 1).

A post-treatment through the hydro−/solvothermal process is essential to pre-crystallize the TiO_2 hydrates to anatase phase *in-situ,* and synchronously fix a highly porous structure with high thermal stability for the subsequent calcination process. Note that the direct calcination without the hydro−/solvothermal post-treatment merely leads to nonporous spheres upon final calcination. Herein we develop a novel microwave-assisted hydrothermal process for the rapid synthesis of MATS. Compared with the conventional hydro−/solvothermal process, the employment of microwave allows for the prompt and uniform heating up, fastening the crystallization process and eventually shortening the hydrothermal time from 8 to 12 h to 0.5 h.

To optimize the hydrothermal temperature (T_h), a control experiment has been conducted to study their textural property revolution in the crystal phase and porous structure. Monitored with XRD technique and BET surface area analysis, we compared the crystal size, crystallinity, surface area, and pore size of different as-hydrothermal products hydrothermally reacted at 110, 130, 160 °C for 0.5 h (see Table S1). The self-template crystallization of HTCS to anatase phase (see Fig. 1a and S1a) is in good agreement with the classic hydrothermal principle: the higher T_c corresponds to the bigger grain size and higher crystallinity. Our calculation using the Scherrer equation from the (101) diffraction peak [57] demonstrates that the crystal size gradually increases from 4.41 to 6.60 and 7.26 nm with the increase in T_h, followed by the enhanced crystallinity from 68.6% to 94.8% and 95.5%. The inevitable crystal growth is accompanied by the gradual elimination of porosity. As shown in Fig. 1b and Fig. S1b, the surface area gradually decreases from 219.7 to 201.0 and 176.4 m^2 g^{-1}, while the mean pore size is enlarged from 3.31 to 6.67 and 7.82 nm.

We selected 130 °C as the optimal T_h since the resultant MATS-130 shows integrated superiority in structural parameters, including small grain size, large surface area, and high crystallinity. To remove the surface organic adsorbates and to further crystallize the spheres, MATS-130 has been calcined in air at different calcination temperatures (T_c) 350–550 °C with their spherical morphology well maintained. Table 1 also shows the structural parameters of MATS-350, 450, 500. In our Rietveld refinements of XRD patterns (Fig. S4), the crystallinity of MATS is gradually enhanced by increasing T_c, while the surface area is decreased and pore size is increased due to the gradual crystal growth of anatase TiO_2 (see Table S2). Typically, the TiO_2 nanobuilding blocks in MATS-450 are fully crystallized to anatase at T_c = 450 °C. Further increasing T_c leads to serious crystal fusion and the surface area decreases dramatically to 36.7 m^2 g^{-1} for MATS-550, in contrast to the type-IV isotherm plots with sharp capillary condensation steps of MATS-450 with a large surface area of 88.9 m^2 g^{-1}. As shown in Fig. 2e-h, S2 and S3, the representative SEM and TEM micrographs of MATS-450 display the well-maintained submicrospheres morphology with a rough surface consisting of nanosized anatase nanoparticles after hydrothermal and annealing treatments. The well-assembled anatase grains create a porous structure with enlarged pore size. The high-resolution TEM image in Fig. 2i distinguishes the (101) plane of anatase with a *d*-spacing around 0.35 nm.

3.2. Capacity, rate, and cycling performances and EIS spectra of MATS

Using the elaborated MATS, we assembled the Al|$AlCl_3$/[EMIm]Cl|MATS AIBs. For comparison, Aeroxide P25, comprised of anatase and rutile TiO_2 with a surface area ~ 61.4 m^2 g^{-1}, was also used as referential cathodic materials for the cell assembly [58]. We firstly performed

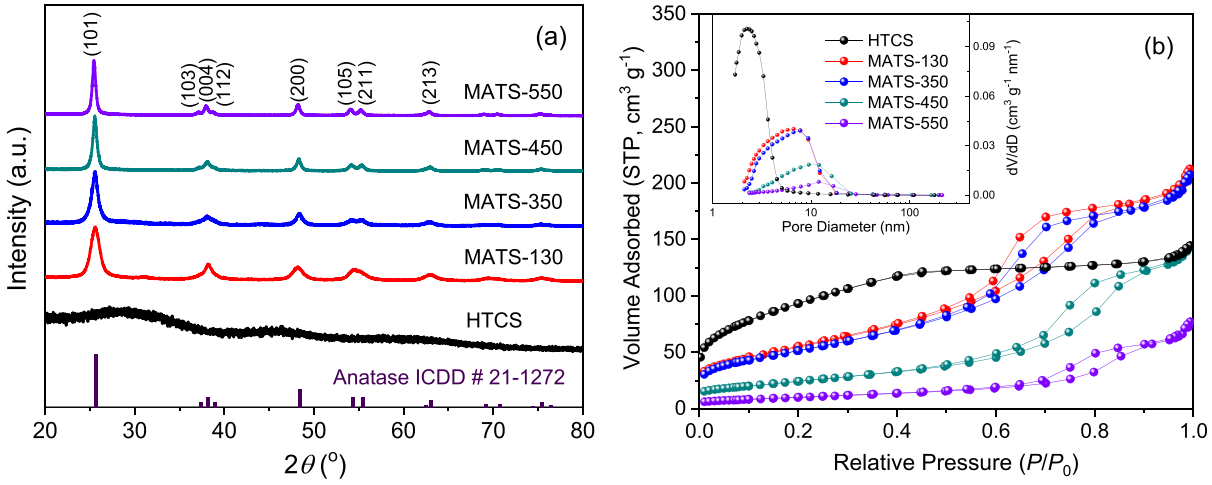

Fig. 1. (a) XRD patterns and (b) N_2 adsorption and desorption isotherms and the pore size distributions obtained from the desorption branches (inset) of HTCS and their MATS products upon the microwave-assisted hydrothermal process at 130 °C (MATS-130) followed with annealing at 350–550 °C (MATS-350-550).

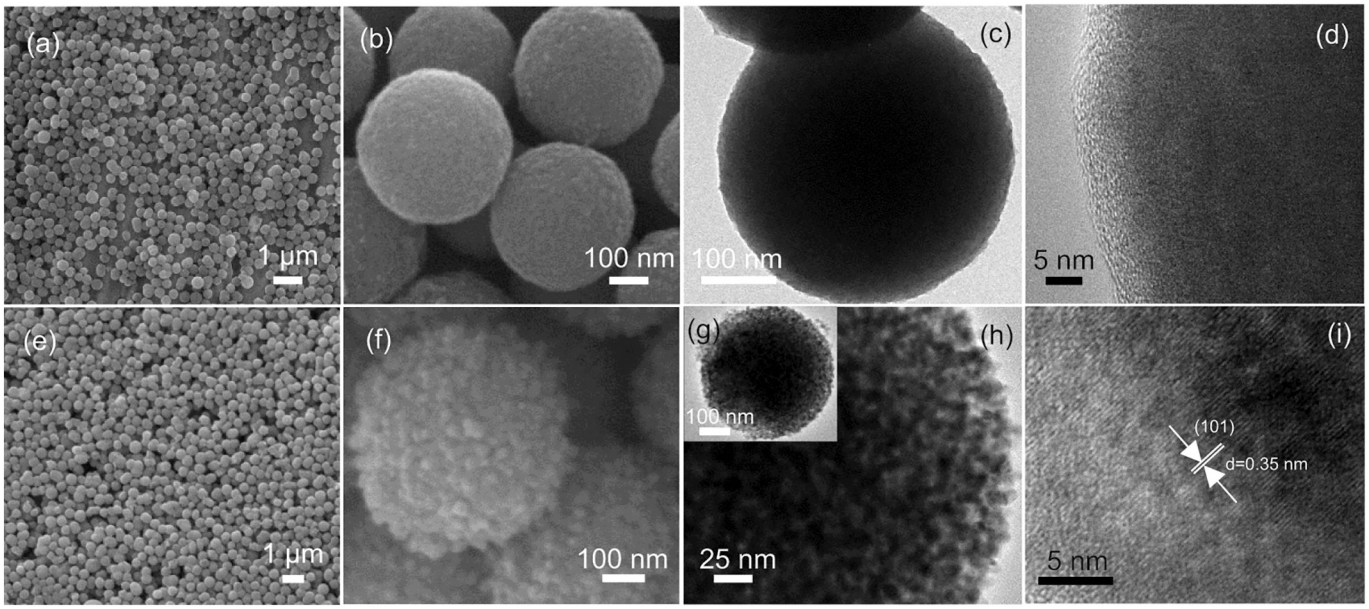

Fig. 2. Comparative SEM and TEM micrographs at different magnifications of (a-d) HTCS and (e-i) MATS-450.

Table 1
Phase and structural parameters of HTCS and MATS.

TiO_2	Grain size (nm)	Crystallinity (%)	Surface area ($m^2\ g^{-1}$)	Pore size (nm)	Pore volume ($cm^3\ g^{-1}$)
HTCS	–	0	337.3	3.12	0.0143
MATS-130	6.60	94.82	201.0	6.67	0.0108
MATS-350	14.2	96.05	187.1	7.80	0.0107
MATS-450	18.0	99.85	88.9	9.51	0.0100
MATS-550	22.4	99.98	36.7	12.0	0.0032

galvanostatic charge/discharge experiments to evaluate the Al ion storage capacities of MATS. Fig. 3a shows the initial charge/discharge profiles of MATS and P25 at 0.2C in the range of 0.2–2.4 V (*vs.* Al/Al^{3+}), respectively. Except for MATS-550, all MATS samples show higher specific capacities and voltage platforms, compared with P25 (≈67.7 mA h g^{-1}), suggesting the beneficial effects of large surface area and porous structure for efficient Al ion storage. Among them, MATS-450 displays the highest discharge capacity of ≈145.3 mA h g^{-1} with a Coulombic efficiency of ≈96.5% and a stable charge/discharge platform at ≈2.20/1.47 V, respectively.

Fig. 3b compares their rate performances within 0.2–2.4 V (*vs.* Al/Al^{3+}) at 0.2–5C. Again, MATS-450 possesses the best rate performance of Al ion storage capacities. Even at 2C, it delivers the highest discharged capacity of ≈58.9 mA h g^{-1}, which is over three times higher than that of P25, ≈18.7 mA h g^{-1}. Long-term cycling stabilities of the above samples were assessed at 1C as Fig. 3c shows. MATS-450 presents an impressive initial discharge capacity of ≈118.3 mA h g^{-1} and remains at 78.0 mA h g^{-1} with a Coulombic efficiency of ≈98.6% after 200 cycles. According to our literature review (Table S3) on the AIBs using TiO_2 cathodes, our MATS-450 is one of the best electrochemical performances among different TiO_2-based materials.

The Al storage kinetics of MATS and P25 were studied by the EIS technique. After a three-cycle charge/discharge process at 0.2C, the Al|$AlCl_3$/[EMIm]Cl|(MATS or P25) cells were finally discharged to the voltage platform of ≈1.5 V. Fig. 4a shows the Nyquist plots and the fitting results with their equivalent circuit model in the inset. The real part of the Nyquist plot can be expressed as:

$$Z' = R_e + R_{ct} + \sigma_w \omega^{-1/2} \quad (1)$$

where R_e is the electrolyte solution resistance, R_{sei} is the combined resistance of the solid electrolyte interface (SEI) layer, R_{ct} is the charge transfer resistance, *CPE*1 and *CPE*2 are the two constant phase elements, and Z_w represents the Warburg impedance. Table S4 summarizes our EIS fitting results for MATS and P25. The value of R_{ct} follows an incremental order of MATS-450 < MATS-350 < MATS-130 < P25 < MATS-550. As shown in Fig. 4b, the Warburg factor (σ_w), which is related to the mass transport, can be obtained from the slope between Z' and $\omega^{-1/2}$. ω ($2\pi f$) is the angular frequency in the low-frequency region.

The relationship of Al ion species diffusion coefficient (D_{Al}) and σ_w can be expressed as:

$$D_{Al} = R^2T^2 / \left(2A^2n^4F^4c_{Al}{}^2\sigma_w{}^2\right) \quad (2)$$

where R is the gas constant (8.314 J mol^{-1} K^{-1}), T is the measurement temperature (298.15 K), A is the contact area between electrode and electrolyte (1.13 cm^2), n is the number of electrons, F is the Faraday constant, and c is the molar concentration of Al species. It is difficult to determine the value of n and c, due to more than one effective ion. However, D_{Al} and $\sigma_w{}^2$ are inversely proportional; namely, the lower value of σ_w, the higher value of D_{Al}. MATS-450 possesses the lowest value of σ_w as shown in Table S4, which further demonstrates their rapid diffusion kinetics of Al ion species.

The superiority of MATS-450 in capacity, rate, and cycling performances can be primarily attributed to their excellent textural properties appropriate for efficient Al storage: 1) low R_{ct} due to the high crystallinity and spherically assembled nanocrystalline with fewer grain boundaries; 2) large surface area with a larger amount of active sites for high-capacity Al storage; 3) porous structure providing easy paths for Al^{3+} ions with an enhanced D_{Al} for rate performance; 4) spherical morphology with excellent structural stability in the cycling charge/discharge process (see SEM analysis below).

3.3. CV and Galvanostatic intermittent titration technique (GITT) analyses

Fig. 5a shows the CV curves of MATS-450 from the 1st to 3rd cycle recorded at a potential scan rate of 0.1 mV s^{-1} in the range of 0.2–2.4 V

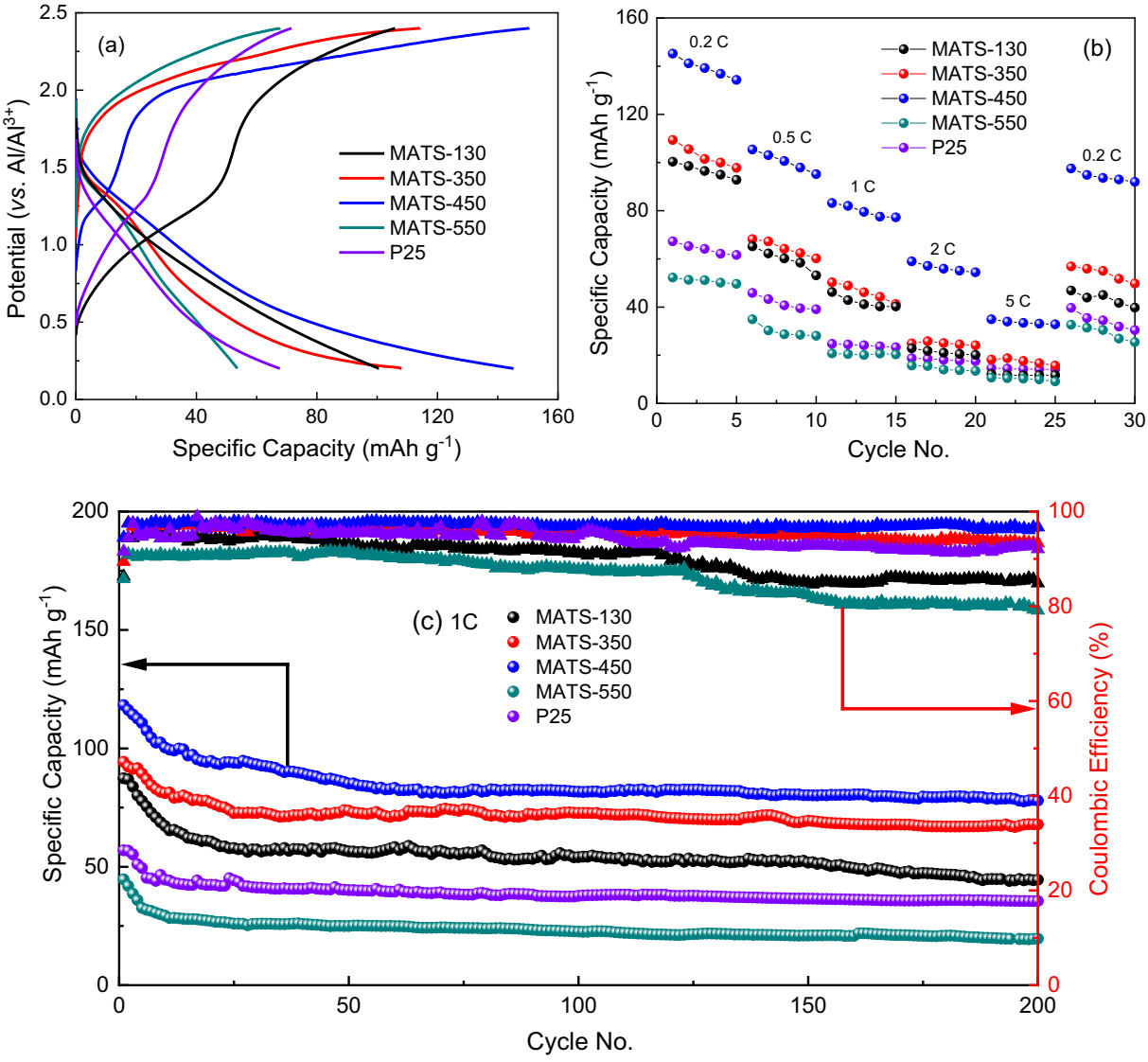

Fig. 3. (a) Initial charge-discharge curves at 0.2C, (b) rate capability, and (c) cycling performances at 1C of P25 and the different MATS samples in the range of 0.2–2.4 V (*vs.* Al/Al^{3+}).

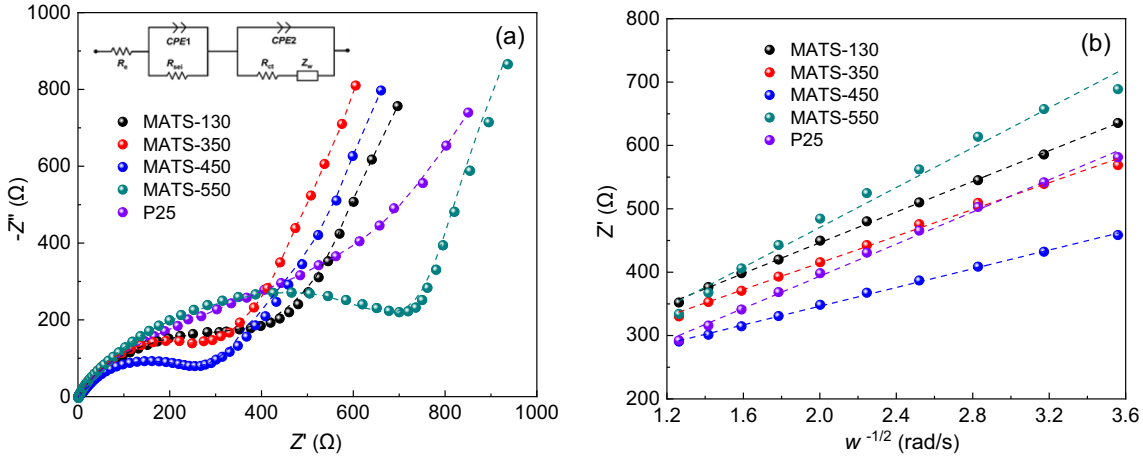

Fig. 4. (a) The Nyquist plots and their fitting results (dotted lines) after three cycles with their equivalent circuit (inset); (b) the relationship between Z' and $\omega^{-1/2}$ for the MATS and P25 cathodes of NAIBs.

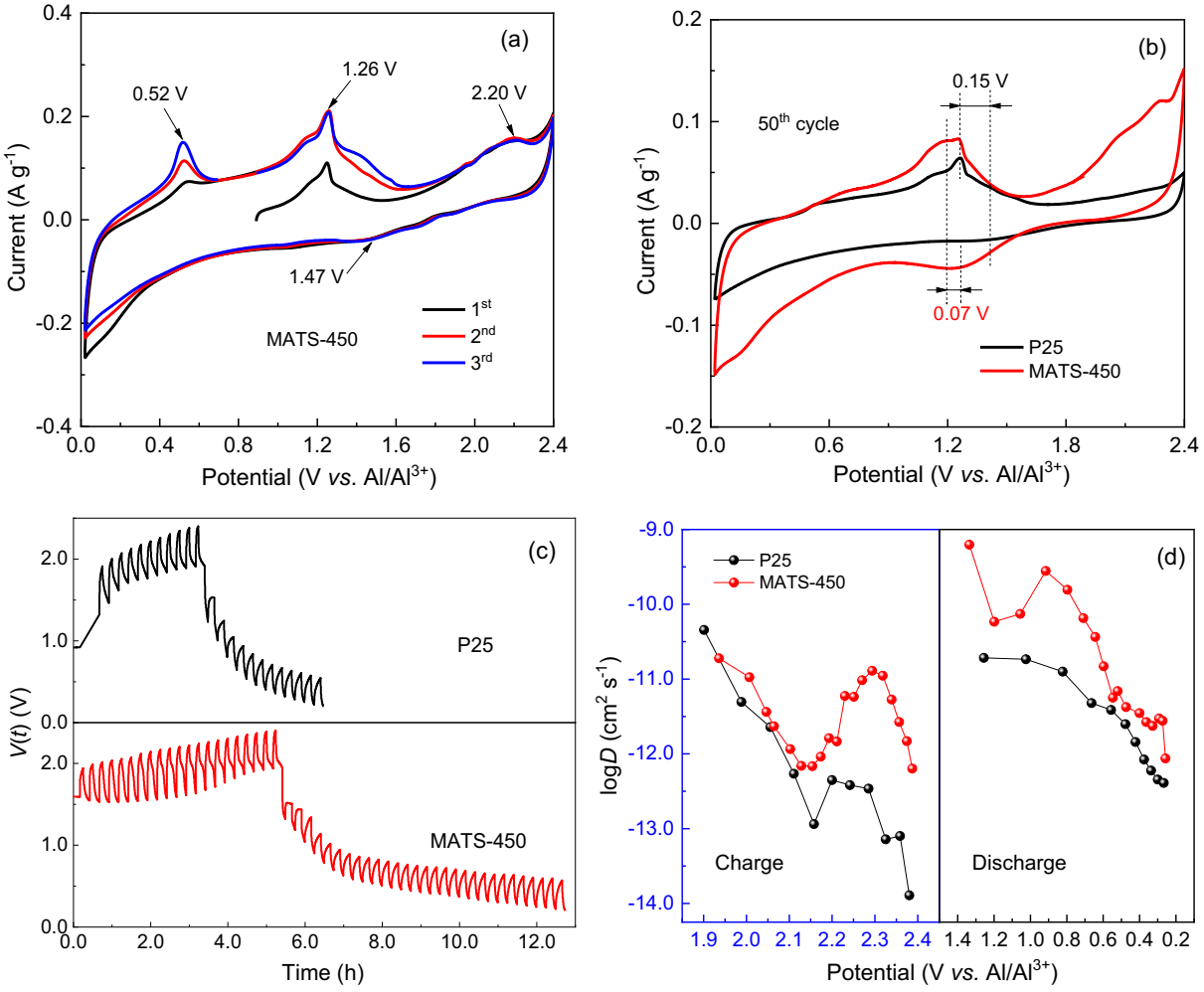

Fig. 5. CV curves of (a) MATS-450 at the first three cycles, and (b) MATS-450 and P25 after 50 cycles, measured at a rate of 0.1 mV s^{-1} and a scan range of 0.2–2.4 V (*vs.* Al/Al^{3+}); (c) charge/discharge GITT curves for MATS-450 and P25 at 0.2C; (d) corresponding Al ion species coefficients during the 5th charge and discharge processes at room temperature for P25 and MATS-450.

(*vs.* Al/Al^{3+}). Interestingly, the solid-electrolyte interface (SEI) layer is almost formed during the first three cycles. The peak location of other oxidation peaks of ≈1.26/2.20 V and the reduction peak at ≈1.47 V are consistent with the voltage platform in the charge/discharge curves in Fig. 3a. No significant peak shift and intensity variation occur, indicating the high reversible insertion/extraction ability of Al^{3+} ions. The corresponding oxidation peak of ≈0.52 V is gradually enhanced, which is related to the underpotential deposition of Al of the cathode and anode.

We also recorded and compared the CV curves of MATS-450 and P25 after the $Al|AlCl_3/[EMIm]Cl|$(P25 or MATS) cells were charged/discharged 50 cycles. The potential difference (φ_p) between the cathodic and anodic peaks can significantly suggest the degree of polarization for the electrode during the cyclic process. As shown in Fig. 5b, MATS-450 exhibits a smaller value of $\varphi_p = 0.07$ V than P25 (0.15 V), together with a pair of better-resolved redox peaks. It can demonstrate that the significantly weaker polarization benefits from the higher surface area and more excellent electrochemical performance of MATS-450 as mentioned before.

Galvanostatic intermittent titration technique (GITT) was conducted to further understand the difference in the electrochemical diffusion coefficient of Al ion species in the P25 and MATS samples. Fig. 5d shows the chemical diffusion coefficients of Al ion species in P25 and MATS-450 as a function of voltage for the 5th cycle with a constant current density of 0.2C and each pulse lasts 300 s followed by 600 s of rest. As shown from Fig. 5c, MATS-450 takes a longer time for Al ion species to reach a steady state and possesses a larger capacity, compared with those of P25. The GITT diffusivity of the studied TiO_2 cathodic materials can be expressed as [59]:

$$D_{Al} = \frac{4}{\pi\tau}\left(\frac{m_B V_m}{M_B A}\right)^2 \left(\frac{\Delta V_s}{\Delta V_t}\right)^2 \quad (\tau \ll L^2/D_{Al}) \tag{3}$$

where τ is the time duration of the pulse; m_B, V_m, and M_B are the active mass, molar volume, and molecular weight of TiO_2, respectively; A is the cell interfacial area; L is the thickness of the electrode; ΔV_s means the change in the steady-state voltage during the respective single titration; and ΔV_t is the total transient change in cell voltage after subtracting the IR drop. As calculated from Fig. 5d, the D_{Al} values of MATS at the 5th charge/discharge cycle are determined to be in the range of $10^{-9.0}$ to $10^{-12.5}$ cm^2 s^{-1}, all of which are higher than those of P25 ($10^{-10.5}$ to $10^{-14.0}$ cm^2 s^{-1}). Typically, the D_{Al} values at the charge and discharge states are closer for MATS-450, further suggesting its higher performances in the reversible electrochemical insertion/extraction of Al ion species.

3.4. Pseudocapacitive analysis of MATS

Pesudocapacitive analysis is adopted to investigate the behavior of MATS-450 for AIB. As shown in Fig. 6a, the CV analyses were carried out

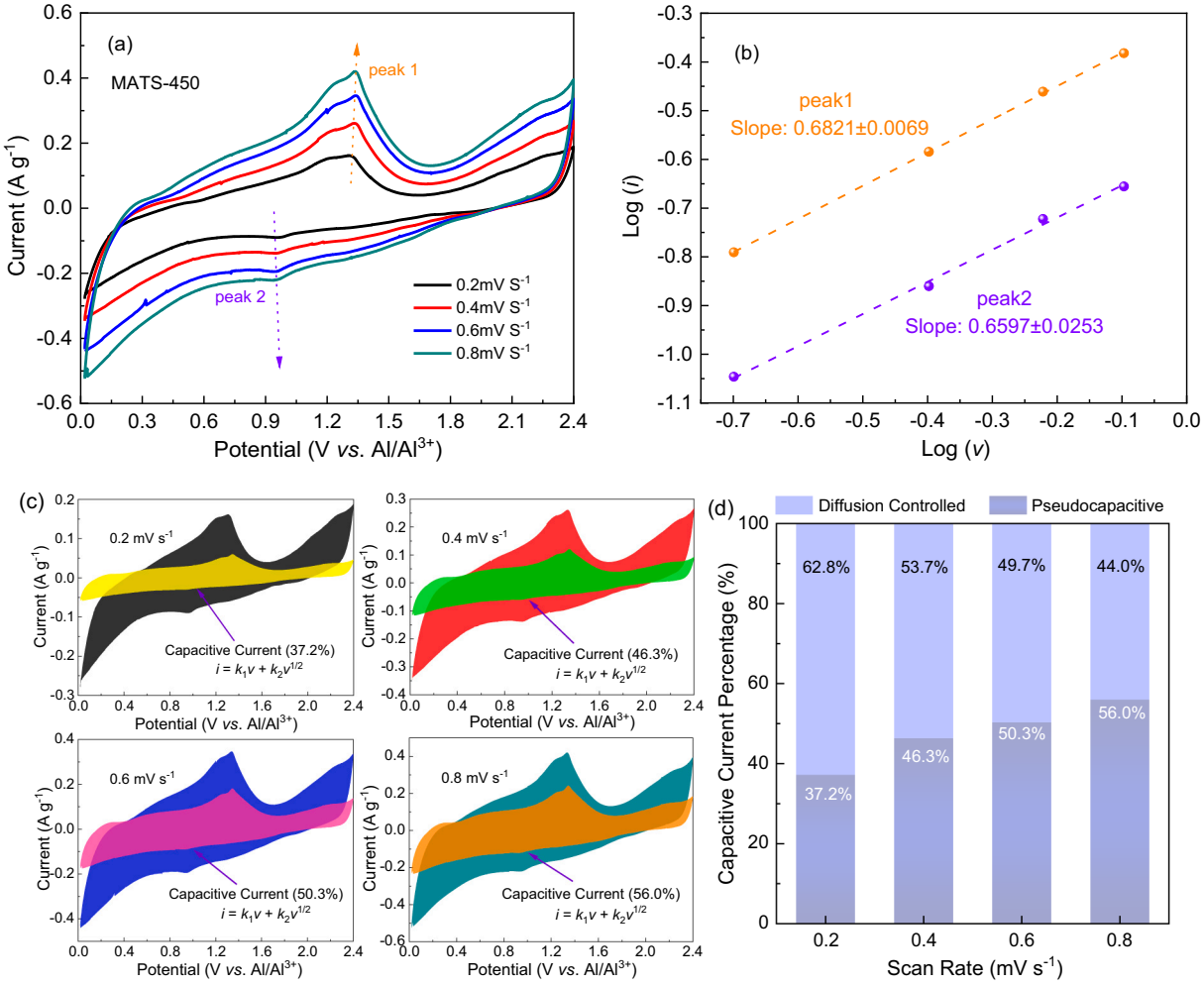

Fig. 6. The CV curves at various scan rates and their derived pseudocapacitive analysis of the MATS-450: (a) CV curves at 0.2–0.8 mV s^{-1}; (b) their linear relationship between log (*i*)-log (*v*); and (c) their contribution ratio of the capacitive capacities and diffusion-limited capacities and (d) the corresponding bar diagram.

at various scan rates from 0.2 to 0.8 mV s^{-1} between 0.2 and 2.4 V (*vs.* Al^{3+}/Al). A pair of reversible oxidation and reduction peaks can be observed around 1.34 V and 0.95 V *vs.* Al/Al^{3+}. With the increasing scan rate, the peak current (*i*) at a certain potential is not proportional to the square root of the scan rate (*v*), indicating that the oxidation and reduction processes are controlled by both pseudocapacitance characteristics and ion diffusion [20]. Here, the relationship between *i* and *v* can be described by the following equations:

$$i = av^b, (0.5 \le b \le 1) \quad (4)$$

$$logi = blogv + loga \quad (5)$$

where *a* and *b* are variable parameters. The *b* value is always adopted to investigate the Al^{3+} storage behavior. Particularly, $b = 1$ means the completely capacitive characteristics-controlled process, whereas $b = 0.5$ stands for the completely diffusion-controlled one. The *b* value of peak 1 and peak 2 of MATS-450 is 0.6821 and 0.6597 with the error value of the 0.0069 and 0.0253 from the log*i*-log*v* relationship (Fig. 6b), demonstrating that the MATS-450 based AIB energy storage is dominated by a diffusion-controlled process.

Since the energy storage of the MATS-450-based AIB possesses the both pseudocapacitance and ion diffusion characteristics. Fig. 6c summarizes their contribution ratio by using the following equations:

$$i = k_1v + k_2v^{1/2} \quad (6)$$

where k_1 and k_2 are adjustable constants, and $k_1\nu$ and $k_2\nu^{1/2}$ represent the capacitive-controlled contribution and the Al ion species diffusion-controlled contribution in MATS-450, respectively. As calculated from Fig. 6d, the percentage of pseudocapacitance at 0.2, 0.4, 0.6, and 0.8 mV s^{-1} is 37.2%, 46.3%, 50.3%, and 56.0%, and the thus corresponding percentage of diffusion-controlled contribution is 62.8%, 53.7%, 49.7%, and 44.0%, respectively. Notably, the pseudocapacitance-controlled contribution of 56.0% at 0.8 mV s^{-1}. The pseudocapacitance gradually dominates the battery energy storage as the scan rate increase.

3.5. Al^{3+} storage mechanism of MATS in NAIBs

Attempts have been made to reveal the underlying Al insertion/extraction mechanism of MATS cathodes in NAIBs. Our interest was mainly directed to phase and composition evolution in MATS during the charge/discharge process [35,53,56]. Thus, we disassembled the tested NAIBs after 50 cycles at 0.5C, and two MATS-450 cathodes were collected at their charging and discharging states, respectively. For comparison, the pristine cathode without any electrochemical cycle was immersed in $AlCl_3$/[EMIm]Cl electrolyte for 12 h. All these three cathodes were subjected to sufficient wash with MeCN to eliminate the physically adsorbed Al species on the MATS cathodes before the subsequent *ex-situ* SEM-EDX and XPS measurements.

The SEM-EDX technique provides a statistical and straightforward tool to compare the changes in morphology and surface composition of

MATS after being charged and discharged. Fig. 7 depicts their SEM micrographs and the corresponding EDX elemental mappings of MATS-450. The spherical morphology and hierarchical structure of MATS-450 are well reserved after 50 cycles by comparing the top-view micrographs. EDX elemental mapping shows that all three samples exhibit regions containing a dominant Ti signal due to the presence of MATS-450.

The signals for Al and Cl elements in the pristine MATS-450 are extremely weak due to the absence of electrochemical reaction but physical adsorption of ions occurring on the cathode merely (Fig. 7a). Hence, the adsorbed Al and Cl species are negligible after MeCN washing. As clearly shown in Fig. 7b and c, the stronger signals of Al and Cl elements in both charged and discharged MATS-450 cathodes are originated from the insertion of Al^{3+} and Cl^{-} ions into the crystal lattices of anatase TiO_2 and probably the SEI layer containing Al^{3+} and Cl^{-} ions. Compared with charged counterpart, the discharged MATS-450 cathode (Fig. 7c) is almost entirely covered with Al and Cl elements. The signal enhancements are contributed from the electrochemical insertion of Al and Cl species (*e.g.* Al^{3+}, $AlCl_4^{-}$ or $Al_2Cl_7^{-}$ *etc.*) into TiO_2. For the charged sample, a certain amount of Al and Cl elements in MATS-450 cathode (Fig. 7b) might be assigned to the presence of SEI and the resident Al and Cl species. Surely the latter is inactive in Al insertion/extraction and results in the deteriorated electrochemical reversibility and poor-rate and capacity performances of NAIBs.

We further performed *ex-situ* XPS analysis to identify the surface composition and oxidation state of Ti, Al, Cl elements in the MATS-450 cathode during the charge/discharge process. Fig. 8 shows XPS survey spectra and high-resolution XPS spectra of Ti 2p, Al 2p, and Cl 2p recorded on the pristine, charged, and discharged MATS-450 cathodes. As shown in Fig. 8b, there is only one peak of Ti^{4+} at 459.8 eV in the pristine sample. Upon charge and discharge, two peaks at 459.5 and 459.9 eV can be well resolved, indicating the co-existing of Ti^{4+} and Ti^{3+} species during the redox process. Relatively, the discharge induced the richer Ti^{3+} species whose XPS peaks locate at the lower binding energy. Hence, Ti^{4+} is reduced to Ti^{3+} during the discharge process; while Ti^{3+} is oxidized back to Ti^{4+} during charge. Al 2p and Cl 2p peaks appear upon the charge/discharge process followed by the electrochemical Al insertion/extraction on the MATS-450 side. An intense peak at 75.4 eV corresponding to the Al^{3+} can be clearly observed in Al 2p (Fig. 8c), which verifies Al^{3+} insertion into MATS-450 during discharging process; while two pairs of peaks (at (197.8 and 199.0 eV) and (199.6 and 201.1 eV)) can be assigned to the spin-orbit split $2p_{1/2}/2p_{3/2}$ components for $AlCl_4^{-}$ and Cl^{-} are observed in Cl 2p (Fig. 8d), respectively [60]. The Al and Cl areas of the discharged electrode are ≈2 times larger than those of charged cathode. The enrichments in Al and Cl species, in good agreement with the SEM-EDX results, further verify the involvement of Al species (Al^{3+}, $AlCl_4^{-}$, $Al_2Cl_7^{-}$, etc) in the electrode reaction. The presence of Al and Cl signals in the charged sample may be due to the side reactions between $AlCl_3$/[EMIm]Cl electrolyte with PVDF in the electrode [61].

Table 2 summarizes the molar ratio of Ti, Al, and Cl of MATS-450 at the initial, charged, and discharge states, revealed by the XPS technique. Note that such quantitative analysis is not very accurate but able to, to some extent, reflect the reversible extraction/insertion of Al^{3+} in TiO_2 during the charge/discharge process. The discharge significantly increases the amounts of both Al and Cl elements in TiO_2, which then decrease during the charging process. We normalize the amount of Ti to 1 mol, and the molar ratio of Al/Cl keeps less than 1, namely, ≈1/3 (0.21/0.58) for the pristine with $AlCl_3$ adsorbed ≈2/3 (0.50/0.75), and ≈3/3 (1.48/1.52) at charged and discharged states, which clearly indicates that the Al ion transportation is accompanied with the movement of Cl species. If we assume that, after being charged, the remaining Al and Cl species are resident, we also can image a larger amount of Al (*i.e.* 1.48–0.50) shuttle between the Al and TiO_2 electrodes, compared with Cl (1.52–0.75). The shutting ions can be denoted as $AlCl_{1-x}$. Thus, it seems that Al^{3+} would be a key effective ion for Al ion storage, although co-existing $AlCl_4^{-}$ or $Al_2Cl_7^{-}$ ions can not be negligible. Future works will be performed to investigate the exact ions, their proportion, and evolution during working in NAIBs.

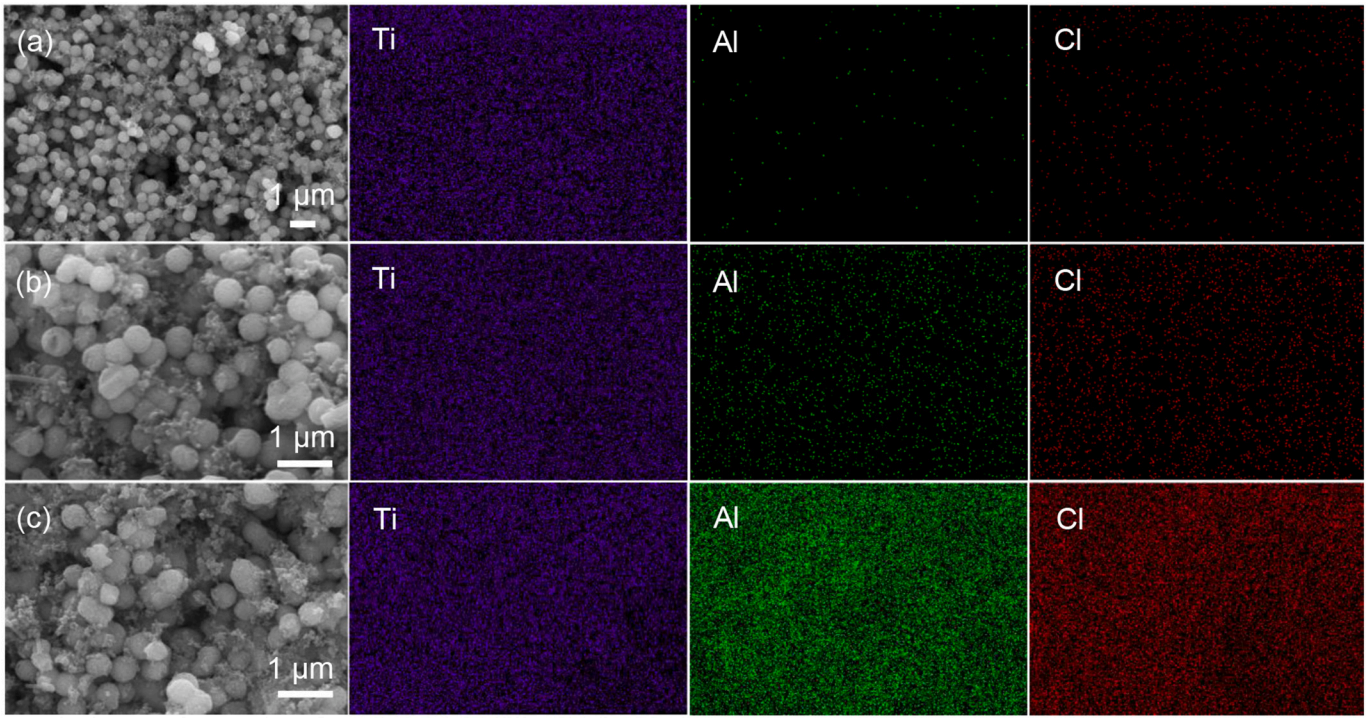

Fig. 7. SEM micrographs with corresponding EDX elemental mappings of (a) pristine without cycling, (b) charged and (c) discharged MATS-450 cathodes obtained after 50 cycles.

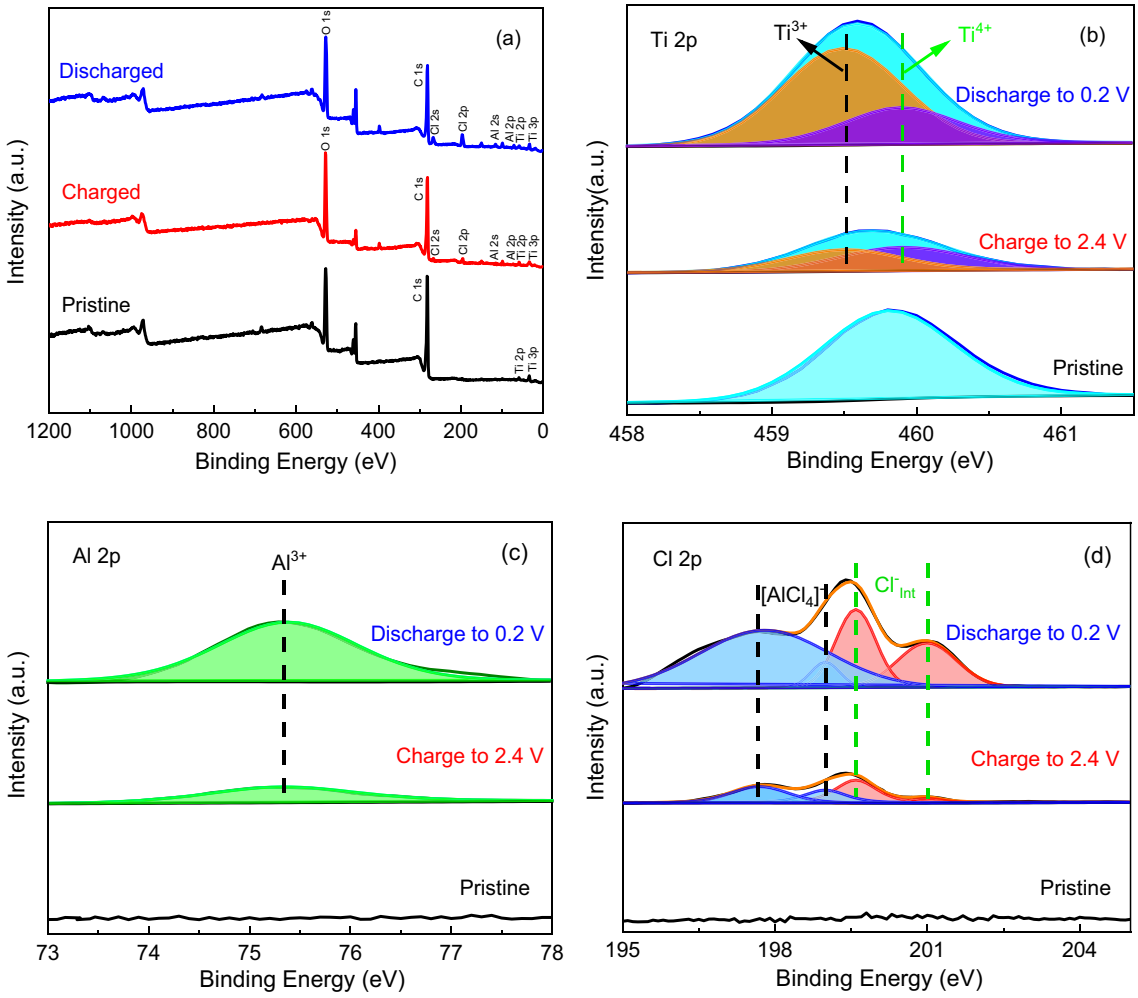

Fig. 8. (a) *Ex-situ* XPS survey of pristine (black), charged (red), and discharged (blue) MATS-450 cathodes after 50 cycles, and their corresponding high-resolution XPS spectra of (b) Ti 2p, (c) Al 2p, and (d) Cl 2p.

Table 2
The quantitative XPS analyses of Ti, Al, and Cl molar ratios of the pristine, charged and discharged MATS-450 cathodes.

MATS-450	Ti	Al	Cl
Pristine	1	0.21	0.58
Charged	1	0.50	0.75
Discharged	1	1.48	1.52

3.6. Long-term stability of MATS and performance degradation mechanism

The *ex-situ* XRD analysis is performed to further explore the underlying phase transitions of the MATS-450 cathode during the Al insertion/extraction process at charge/discharge states and different cycles (*i.e.* 50th, 200th, and 600th). Fig. 9 summarizes their XRD analysis results. The pristine MATS-450 cathode (black) shows a typical anatase phase with a space group $I4_1/amd$. The prominent diffraction peak at 2θ of 58.6° and the other two small peaks at 40.4° and 52.4° can be assigned to the current collector of metallic Mo (ICDD 42–1120). After 50 cycles, four new phases can be resolved in the discharged sample (blue), which can be indexed as $Al_2Ti_7O_{15}$ (ICDD #39–0052); Al_2TiO_5 (ICDD #70–1435); $Ti(AlCl_4)_2$ (ICDD #25–0980); and $Ti(ClO_4)_4$ (ICDD #32–1367). These four intermediate phases are absent in the charged counterpart (red), suggesting a fairly reversible crystal phase transition during the cyclic Al^{3+} insertion/extraction process. Tracing back to the source, the $Al_2Ti_7O_{15}$, Al_2TiO_5, and $Ti(AlCl_4)_2$ phases are generated due to the insertion of Al^{3+} ions into MATS [39]; while the $Ti(ClO_4)_4$ phase might be derived from the side reaction of PVDF with $AlCl_3$/[EMIm]Cl electrolyte. Note that the insertion of Al^{3+} leads to a dramatical increase in the lattice volumes, *i.e.* 136.38, 326.30, 486.22 and 1177.23 Å^3 for anatase TiO_2, $Al_2Ti_7O_{15}$, $Al_2Ti_7O_{15}$ and $Ti(AlCl_4)_2$, respectively. Therefore, the porous structure of MATS is helpful to accommodate the volume expansion during the insertion of Al^{3+} ions into the anatase TiO_2 crystal lattices.

It is well known that AIBs keep in service far shorter than LIBs. To understand the performance degradation mechanism of AIBs, we extended the charge/discharge cycles and measured the XRD patterns of MATS-450 cathodes after 200 and 600 cycles. As also shown in Fig. 9, the deterioration in the cathode and the degradation in electrochemical performances are clearly evident in the crystal phase evolution of MATS-450. After 200 cycles, the $Al_2Ti_7O_{15}$, Al_2TiO_5, $Ti(AlCl_4)_2$, and $Ti(ClO_4)_4$ phase becomes dominant, in contrast to the co-existed TiO_2 phase. Certainly, these four phases are inactive in Al^{3+} insertion/exsertion reactions, and merely the remaining anatase TiO_2 might take part in the electrochemical reactions. Thus, the difference in the XRD patterns between the charged and discharged samples is greatly reduced.

The phase transition from anatase TiO_2 to unactive Ti-containing phases is continuously developed. After 600 cycles, anatase TiO_2 has been a minor phase. Non-oxide phases, $Ti(AlCl_4)_2$ and $Ti(ClO_4)_4$ become dominant as their peak intensities rapidly strengthen with the conduction of the cycling process, and show slight variation in the peak

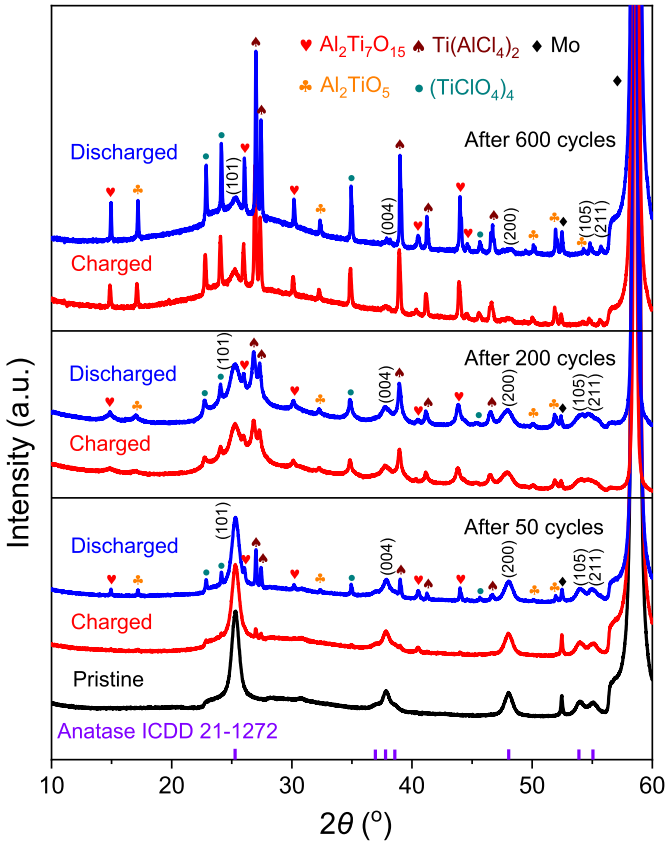

Fig. 9. *Ex-situ* XRD patterns of pristine (black), charged (red), and discharged (blue) MTS-450 cathodes after 50, 200 and 600 cycles at 1C between 0.2 and 2.4 V (*vs.* Al^{3+}/Al).

intensity during the charge/discharge process. Thus, this irreversible phase transition dramatically lowers the reversibility and eventually worsens the electrochemical performances of NAIBs, resulting in a significant loss in the specific captivity: after 600 cycles, ≈ 32.8 mA h g^{-1} with low Coulombic efficiency of ≈90.7% is remained, as shown in Fig. S5.

3.7. Working principle of AIBs with MATS cathode

Based on the above discussion, a schematic diagram for the working principle of Al|$AlCl_3$-[EMIm]Cl|MATS battery is illustrated in Scheme 1. As proposed previously [20,49], the underlying reversible electrochemical reactions on the Al anode and TiO_2 cathode can be written as follows. Note that both the forward reactions describe the discharge process in NAIBs.

$$\text{Anode}: 7x\text{AlCl}_4^- + x\text{Al} - 3xe^- \leftrightarrow 4x\text{Al}_2\text{Cl}_7^- \quad (7)$$

$$\text{Cathode}: 4x\text{Al}_2\text{Cl}_7^- + \text{TiO}_2 + 3xe^- \leftrightarrow \text{Al}_x\text{TiO}_2 + 7x\text{AlCl}_4^- \quad (8)$$

During the discharge process (red clockwise closed loop in Scheme 1), Al anode is prone to oxidization in the $AlCl_3$/[EMIm]Cl electrolyte. The released Al^{3+} ions can react with the $AlCl_4^-$ readily, partially generating $Al_2Cl_7^-$ ions. $Al_2Cl_7^-$ can decompose into Al^{3+} and $AlCl_4^-$ reversely when $Al_2Cl_7^-$ diffuses to the interface on the cathode side. Clearly, Al^{3+} ions could embed in MATS cathode, forming $Al_2Ti_7O_{15}$ and Al_2TiO_5 [39]. Wu et al. [18] suggested that $AlCl_4^-$ ions can diffuse to the anode side and convert to $Al_2Cl_7^-$ by combining with the dissolved Al^{3+}. However, our finding here shows that $AlCl_4^-$ ions can also insert into the crystal lattices of MATS, generating an additional $Ti(AlCl_4)_2$ phase. As evidenced in XPS and EDX, a considerable amount of Cl elements can be detected on the TiO_2 surface. While in the charging process (black counterclockwise closed loop in Scheme 1), the disassembled Al^{3+} ions from the MATS cathode can be deposited on the Al metal anode side.

4. Conclusions

Textural property-controllable MATS has been successfully elaborated through the microwave-assisted rapid crystallization of HTCS self-template. Tuning the hydrothermal and calcination temperatures allow for tuning the structural parameters of MATS, including grain size, crystallinity, BET specific surface area, and pore size. Our optimized MATS-450 has been demonstrated as a promising cathode material for NAIBs with superior rate and capacity performances: the constructed NAIBs with RTIL electrolyte of $AlCl_3$/[EMIm]Cl deliver an initial capacity of 145.3 mA h g^{-1} at 0.2C, and a reversible capacity of 78.0 mA h g^{-1} at 1C can be retained after 200 cycles with a high Coulombic efficiency of ≈98.6%. Our storage mechanism study demonstrates the charge/discharge process mainly involves the extraction/insertion of Al^{3+} and $AlCl_4^-$ ions with the formation of intermediate aluminium titanium oxides ($Al_2Ti_7O_{15}$ and Al_2TiO_5), while the concomitantly

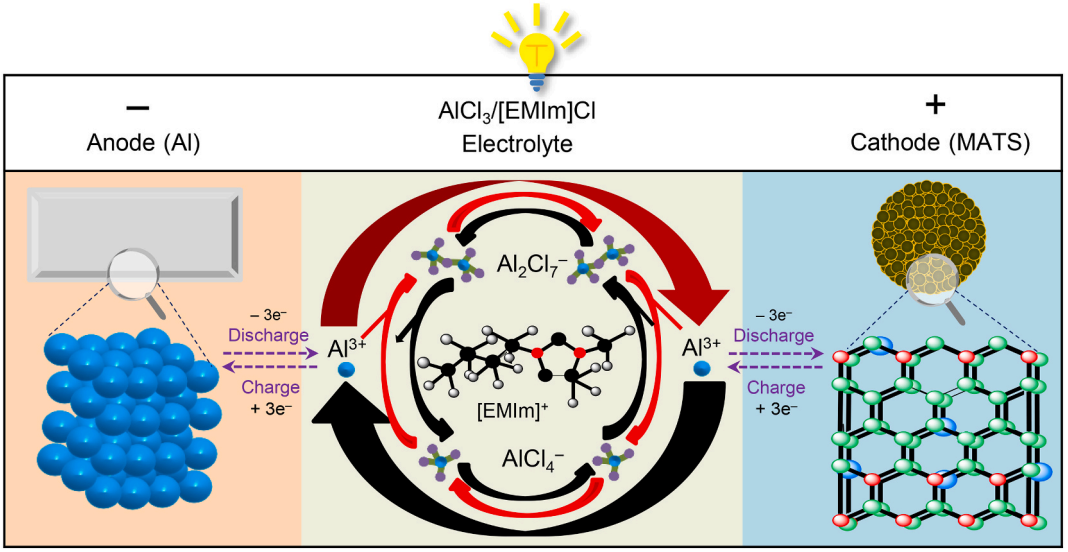

Scheme 1. Schematic illustration of the reaction mechanism of NAIBs with MATS cathode material and $AlCl_3$/[EMIm]Cl electrolyte.

generated non-oxides of $Ti(AlCl_4)_2$ and $Ti(ClO_4)_4$ generated concomitantly show poor eletrochemical reversibility and thus reduces the cycling performance of NAIBs.

Declaration of Competing Interest

The authors declare no competing financial interest.

Acknowledgments

This work is supported by the National Natural Science Foundation of China (No. 52076074).

Appendix A. Supplementary data

Supplementary data to this article can be found online at https://doi.org/10.1016/j.susmat.2022.e00419.

References

[1] H. Kim, W. Choi, J. Yoon, J.H. Um, W. Lee, J. Kim, J. Cabana, W.S. Yoon, Exploring anomalous charge storage in anode materials for next-generation Li rechargeable batteries, Chem. Rev. 120 (2020) 6934–6976.
[2] E. Fan, L. Li, Z. Wang, J. Lin, Y. Huang, Y. Yao, R. Chen, F. Wu, Sustainable recycling technology for Li-ion batteries and beyond: challenges and future prospects, Chem. Rev. 120 (2020) 7020–7063.
[3] Y. Sui, C. Liu, R.C. Masse, Z.G. Neale, M. Atif, M. AlSalhi, G. Cao, Dual-ion batteries: the emerging alternative rechargeable batteries, Energy Storage Mater. 25 (2020) 1–32.
[4] F. Wu, H. Yang, Y. Bai, C. Wu, Paving the path toward reliable cathode materials for aluminum-ion batteries, Adv. Mater. 31 (2019) 1806510.
[5] A. Ponrouch, C. Frontera, F. Bardé, M.R. Palacín, Towards a calcium-based rechargeable battery, Nat. Mater. 15 (2016) 169–172.
[6] L. Ma, M.A. Schroeder, O. Borodin, T.P. Pollard, M.S. Ding, C. Wang, K. Xu, Realizing high zinc reversibility in rechargeable batteries, Nat. Energy 5 (2020) 743–749.
[7] J. Xie, Q. Zhang, Recent progress in multivalent metal (Mg, Zn, Ca, and Al) and metal-ion rechargeable batteries with organic materials as promising electrodes, Small 15 (2019) 1–20.
[8] Y. Wu, H. Zhao, Z. Wu, L. Yue, J. Liang, Q. Liu, Y. Luo, S. Gao, S. Lu, G. Chen, X. Shi, B. Zhong, X. Guo, X. Sun, Rational design of carbon materials as anodes for potassium-ion batteries, Energy Storage Mater. 34 (2021) 483–507.
[9] H. Yang, F. Wu, Y. Bai, C. Wu, Toward better electrode/electrolyte interfaces in the ionic-liquid-based rechargeable aluminum batteries, J. Energy Chem. 45 (2020) 98–102.
[10] L. Zheng, H. Yang, Y. Bai, C. Wu, Designing electrode materials for aluminum-ion batteries towards fast diffusion and multi-electron reaction, J. Energy Chem. 60 (2021) 229–232.
[11] X. Zhang, S. Jiao, J. Tu, W.L. Song, X. Xiao, S. Li, M. Wang, H. Lei, D. Tian, H. Chen, D. Fang, Rechargeable ultrahigh-capacity tellurium-aluminum batteries, Energy Environ. Sci. 12 (2019) 1918–1927.
[12] H. Yang, H. Li, J. Li, Z. Sun, K. He, H. Cheng, F. Li, The rechargeable aluminum battery: opportunities and challenges, Angew. Chem. Int. Ed. 58 (2019) 11978–11996.
[13] B. Craig, T. Schoetz, A. Cruden, C. Ponce, D. Leon, Review of current progress in non-aqueous aluminium batteries, Renew. Sust. Energ. Rev. 133 (2020), 110100.
[14] N. Zhu, K. Zhang, F. Wu, Y. Bai, C. Wu, Ionic liquid-based electrolytes for aluminum/magnesium/sodium-ion batteries, Energy Mater. Adv. 2021 (2021) 1–29.
[15] E. Faegh, B. Ng, D. Hayman, W.E. Mustain, Practical assessment of the performance of aluminium battery technologies, Nat. Energy 450 (2020) 6.
[16] M.C. Lin, M. Gong, B. Lu, Y. Wu, D.Y. Wang, M. Guan, M. Angell, C. Chen, J. Yang, B.J. Hwang, H. Dai, An ultrafast rechargeable aluminium-ion battery, Nature 520 (2015) 325–328.
[17] Z. Liu, J. Wang, H. Ding, S. Chen, X. Yu, B. Lu, Carbon nanoscrolls for aluminum battery, ACS Nano 12 (2018) 8456–8466.
[18] S. Jiao, H. Lei, J. Tu, J. Zhu, J. Wang, X. Mao, An industrialized prototype of the rechargeable Al/$AlCl_3$-[EMIm]Cl/graphite battery and recycling of the graphitic cathode into graphene, Carbon 109 (2016) 276–281.
[19] H. Wang, Y. Bai, S. Chen, X. Luo, C. Wu, F. Wu, J. Lu, K. Amine, Binder-free V_2O_5 cathode for greener rechargeable aluminum battery, ACS Appl. Mater. Interfaces 7 (2015) 80–84.
[20] N. Zhu, F. Wu, Z. Wang, L. Ling, H. Yang, Y. Gao, Reversible Al^{3+} storage mechanism in anatase TiO_2 cathode material for ionic liquid electrolyte-based aluminum-ion batteries, J. Energy Chem. 51 (2020) 72–80.
[21] S. Wang, Z. Yu, J. Tu, J. Wang, D. Tian, Y. Liu, S. Jiao, A novel aluminum-ion battery: Al/$AlCl_3$-[EMIm]cl/Ni_3S_2@ graphene, Adv. Energy Mater. 6 (2016) 1600137.
[22] T. Mori, Y. Orikasa, K. Nakanishi, C. Kezheng, M. Hattori, T. Ohta, Y. Uchimoto, Discharge/charge reaction mechanisms of FeS_2 cathode material for aluminum rechargeable batteries at 55°C, J. Power Sources 313 (2016) 9–14.
[23] S. Wang, S. Jiao, J. Wang, H. Sen Chen, D. Tian, H. Lei, D.N. Fang, High-performance aluminum-ion battery with CuS@C microsphere composite cathode, ACS Nano 11 (2017) 469–477.
[24] W. Yang, H. Lu, Y. Cao, P. Jing, X. Hu, H. Yu, A flexible free-standing cathode based on graphene-like $MoSe_2$ nanosheets anchored on N-doped carbon nanofibers for rechargeable aluminum-ion batteries, Ionics 26 (2020) 3405–3413.
[25] Y. Ai, S.C. Wu, K. Wang, T.Y. Yang, M. Liu, H.J. Liao, J. Sun, J.H. Chen, S.Y. Tang, D.C. Wu, T.Y. Su, Y.C. Wang, H.C. Chen, S. Zhang, W.W. Liu, Y.Z. Chen, L. Lee, J. H. He, Z.M. Wang, Y.L. Chueh, Three-dimensional molybdenum diselenide helical nanorod arrays for high-performance aluminum-ion batteries, ACS Nano 14 (2020) 8539–8550.
[26] J.S. Cho, H.S. Ju, J.K. Lee, Y.C. Kang, Carbon/two-dimensional $MoTe_2$ core/shell-structured microspheres as an anode material for Na-ion batteries, Nanoscale 9 (2017) 1942–1950.
[27] L.D. Reed, S.N. Ortiz, M. Xiong, E.J. Menke, A rechargeable aluminum-ion battery utilizing a copper hexacyanoferrate cathode in an organic electrolyte, Chem. Commun. 51 (2015) 14397–14400.
[28] J. Jiang, H. Li, J. Huang, K. Li, J. Zeng, Y. Yang, J. Li, Y. Wang, J. Wang, J. Zhao, Investigation on the reversible intercalation/deintercalation of Al into the novel Li_3VO_4@C microsphere composite cathode material for aluminum-ion batteries, ACS Appl. Mater. Interfaces 9 (2017) 28486–28494.
[29] H. Lu, F. Ning, R. Jin, C. Teng, Y. Wang, K. Xi, D. Zhou, G. Xue, Two-dimensional covalent organic frameworks with enhanced aluminum storage properties, ChemSusChem 13 (2020) 3447–3454.
[30] X. Huo, X. Wang, Z. Li, J. Liu, J. Li, Two-dimensional composite of D-Ti_3C_2T: X@S@TiO_2 (MXene) as the cathode material for aluminum-ion batteries, Nanoscale 12 (2020) 3387–3399.
[31] D. Kong, H. Fan, X. Ding, D. Wang, S. Tian, H. Hu, D. Du, Y. Li, X. Gao, H. Hu, Q. Xue, Z. Yan, H. Ren, W. Xing, β-Hydrogen of polythiophene induced aluminum ion storage for high-performance Al-polythiophene batteries, ACS Appl. Mater. Interfaces 12 (2020) 46065–46072.
[32] H.K. Jheong, Y.J. Kim, J.H. Pan, T.Y. Won, W.I. Lee, Electrochromic property of the viologen-anchored mesoporous TiO_2 films, J. Electroceram. 17 (2006) 929–932.
[33] Q. Xia, N. Jabeen, S.V. Savilov, S.M. Aldoshin, H. Xia, Black mesoporous $Li_4Ti_5O_{12-\delta}$ nanowall arrays with improved rate performance as advanced 3D anodes for microbatteries, J. Mater. Chem. A 4 (2016) 17543–17551.
[34] M. Ni, D. Sun, X. Zhu, Q. Xia, Y. Zhao, L. Xue, J. Wu, C. Qiu, Q. Guo, Z. Shi, X. Liu, G. Wang, H. Xia, Fluorine triggered surface and lattice regulation in anatase $TiO_{2-x}F_x$ nanocrystals for ultrafast pseudocapacitive sodium storage, Small 16 (2020) 2006366.
[35] K. Li, X. Dai, M. Manawan, Q. Wang, J.H. Pan, Unveiling the formation mechanism and phase purity control of nanostructured $Li_4Ti_5O_{12}$ via a hydrothermal process, Cryst. Growth Des. 21 (2021) 5440–5450.
[36] G.A. Elia, K.V. Kravchyk, M.V. Kovalenko, J. Chacón, A. Holland, R.G.A. Wills, An overview and prospective on Al and Al-ion battery technologies, J. Power Sources 481 (2021), 228870.
[37] S. Liu, J.J. Hu, N.F. Yan, G.L. Pan, G.R. Li, X.P. Gao, Aluminum storage behavior of anatase TiO_2 nanotube arrays in aqueous solution for aluminum ion batteries, Energy Environ. Sci. 5 (2012) 9743–9746.
[38] Z. Sun, J.H. Kim, Y. Zhao, F. Bijarbooneh, V. Malgras, Y. Lee, Y. Kang, S.X. Dou, Rational design of 3D dendritic TiO_2 nanostructures with favorable.pdf, J. Am. Chem. Soc. 133 (2011) 19314–19317.
[39] H. Lahan, S.K. Das, An approach to improve the Al^{3+} ion intercalation in anatase TiO_2 nanoparticle for aqueous aluminum-ion battery, Ionics 24 (2018) 1855–1860.
[40] M. Kazazi, Z.A. Zafar, M. Delshad, J. Cervenka, C. Chen, TiO_2/CNT nanocomposite as an improved anode material for aqueous rechargeable aluminum batteries, Solid State Ionics 320 (2018) 64–69.
[41] D.Y. Wang, C.Y. Wei, M.C. Lin, C.J. Pan, H.L. Chou, H.A. Chen, M. Gong, Y. Wu, C. Yuan, M. Angell, Y.J. Hsieh, Y.H. Chen, C.Y. Wen, C.W. Chen, B.J. Hwang, C. C. Chen, H. Dai, Advanced rechargeable aluminium ion battery with a high-quality natural graphite cathode, Nat. Commun. 8 (2017) 14283.
[42] M. Angell, C.J. Pan, Y. Rong, C. Yuan, M.C. Lin, B.J. Hwang, H. Dai, High coulombic efficiency aluminum-ion battery using an $AlCl_3$-urea ionic liquid analog electrolyte, Proc. Natl. Acad. Sci. 114 (2017) 834–839.
[43] N. Canever, N. Bertrand, T. Nann, Acetamide: a low-cost alternative to alkyl imidazolium chlorides for aluminium-ion batteries, Chem. Commun. 54 (2018) 11725–11728.
[44] K.L. Ng, T. Dong, J. Anawati, G. Azimi, High-performance aluminum ion battery using cost-effective $AlCl_3$-trimethylamine hydrochloride ionic liquid electrolyte, Adv. Sustain. Syst. 4 (2020) 2000074.
[45] C. Li, J. Patra, J. Li, P.C. Rath, M.H. Lin, J.K. Chang, A novel moisture-insensitive and low-corrosivity ionic liquid electrolyte for rechargeable aluminum batteries, Adv. Funct. Mater. 30 (2020) 1909565.
[46] H. Xu, T. Bai, H. Chen, F. Guo, J. Xi, T. Huang, S. Cai, X. Chu, J. Ling, W. Gao, Z. Xu, C. Gao, Low-cost $AlCl_3$/Et_3NHCl electrolyte for high-performance aluminum-ion battery, Energy Storage Mater. 17 (2019) 38–45.
[47] D. Ma, D. Yuan, C. Ponce de León, Z. Jiang, X. Xia, J.H. Pan, Current progress and future perspectives of electrolytes for rechargeable aluminium-ion batteries, Energy Environ. Mater. (2021), https://doi.org/10.1002/eem2.12301.
[48] T. Koketsu, J. Ma, B.J. Morgan, M. Body, C. Legein, W. Dachraoui, M. Giannini, A. Demortière, M. Salanne, F. Dardoize, H. Groult, O.J. Borkiewicz, K.W. Chapman, P. Strasser, D. Dambournet, Reversible magnesium and aluminium ions insertion in cation-deficient anatase TiO_2, Nat. Mater. 16 (2017) 1142–1148.

[49] S. Wang, K.V. Kravchyk, S. Pigeot-Rémy, W. Tang, F. Krumeich, M. Wörle, M. I. Bodnarchuk, S. Cassaignon, O. Durupthy, S. Zhao, C. Sanchez, M.V. Kovalenko, Anatase TiO_2 nanorods as cathode materials for aluminum-ion batteries, ACS Appl. Nano Mater. 2 (2019) 6428–6435.
[50] D. Ma, J. Schneider, W. In, J. Hong, Controllable synthesis and self-template phase transition of hydrous TiO_2 colloidal spheres for photo/electrochemical applications, Adv. Colloid Interface Sci. 295 (2021), 102493.
[51] J.H. Pan, Q. Wang, D.W. Bahnemann, Hydrous TiO_2 spheres: an excellent platform for the rational design of mesoporous anatase spheres for photoelectrochemical applications, Catal. Today 230 (2014) 197–204.
[52] J.H. Pan, X.Z. Wang, Q. Huang, C. Shen, Z.Y. Koh, Q. Wang, A. Engel, D. W. Bahnemann, Large-scale synthesis of urchin-like mesoporous TiO_2 hollow spheres by targeted etching and their photoelectrochemical properties, Adv. Funct. Mater. 24 (2014) 95–104.
[53] D. Ma, K. Li, J.H. Pan, Ultraviolet-induced interfacial crystallization of uniform nanoporous biphasic TiO_2 spheres for durable Lithium-ion battery, ACS Appl. Energy Mater. 3 (2020) 4186–4192.
[54] T. Zhao, R. Qian, Y. Tang, J. Yang, Y. Dai, W.I. Lee, J.H. Pan, Controllable synthesis and crystallization of nanoporous TiO_2 deep-submicrospheres and nanospheres via an organic acid-mediated sol-gel process, Langmuir. 36 (2020) 7447–7455.
[55] T. Zhao, R. Qian, G. Zhou, Y. Wang, W.I. Lee, J.H. Pan, Mesoporous WO_3/TiO_2 spheres with tailored surface properties for concurrent solar photocatalysis and membrane filtration, Chemosphere 263 (2021), 128344.
[56] D. Ma, J. Li, J. Yang, C. Yang, M. Manawan, Y. Liang, T. Feng, Y.-W. Zhang, J. H. Pan, Solid-state self-template synthesis of ta-doped $Li_2ZnTi_3O_8$ spheres for efficient and durable lithium storage, iScience 24 (2021), 102991.
[57] A.L. Patterson, The scherrer formula for X-ray particle size determination, Phys. Rev. 56 (1939) 978–982.
[58] X. Jiang, M. Manawan, T. Feng, R. Qian, T. Zhao, G. Zhou, F. Kong, Q. Wang, S. Dai, J.H. Pan, Anatase and rutile in evonik aeroxide P25: Heterojunctioned or individual nanoparticles? Catal. Today 300 (2018) 12–17.
[59] Z. Shen, L. Cao, C.D. Rahn, C.-Y. Wang, Least Squares Galvanostatic Intermittent Titration Technique (LS-GITT) for accurate solid phase diffusivity measurement, J. Electrochem. Soc. 160 (2013) A1842–A1846.
[60] C. Pan, M. Shin, D. Liu, M. Kottwitz, R. Zhang, R.G. Nuzzo, A.A. Gewirth, Energy storage mechanisms in high-capacity graphitic C_3N_4 cathodes for Al-ion batteries, J. Phys. Chem. C 124 (2020) 10288–10297.
[61] D.M. Correia, C.M. Costa, J.C. Rodríguez-Hernández, I. Tort Ausina, L.T. Biosca, C. Torregrosa Cabanilles, J.M. Meseguer-Duenãs, S. Lanceros-Méndez, J.L. Gomez Ribelles, Effect of ionic liquid content on the crystallization kinetics and morphology of semicrystalline poly(vinylidene fluoride)/ionic liquid blends, Cryst. Growth Des. 20 (2020) 4967–4979.